

Consistent multiple-relaxation-time lattice Boltzmann method for the volume-averaged Navier-Stokes equations

Yang Liu¹, Jingchun Min^{1, *}

¹ Department of Engineering Mechanics, Tsinghua University, Beijing 100084, China

*Corresponding author, Email: minjc@mail.tsinghua.edu.cn

Abstract: This paper develops a novel multi-relaxation-time (MRT) lattice Boltzmann method (LBM) for solving the volume averaged Navier-Stokes equations (VANSE). Different from the approach given in [1], this method is rooted in the widely-adopted density equilibrium distribution, which provides possibility for simulating scenarios where fluid compressibility cannot be ignored, e.g., thermal and multiphase flows. The Chapman-Enskog analysis is presented to confirm the consistency of this scheme at macroscopic level. Some numerical experiments further demonstrate that it achieves second-order convergence and exhibits better numerical performance over previous schemes as reported [2-4].

1. Introduction

The volume-averaged Navier-Stokes equations (VANSE), bridging the microscopic interactions with the macroscale flow behavior, serve as the crux for the coarse-grained simulations of fluid-solid multiphase systems [5]. These equations can be derived from the standard Navier-Stokes equations (NSE) via the local averaging technique, which introduces the void fraction to describe the proportions of fluid and solid phases per unit volume disregarding of their detailed interfaces [6]. By upscaling the microstructural effects into theoretical or empirical drag and collision models from the unresolved mesoscopic perspective, several multiphase approaches rooted in VANSE have garnered substantial attention in recent years for their computational efficiency and satisfactory accuracy in particulate tracking [7]. For dispersed multiphase flows, VANSE are integral to two prevalent frameworks: the two-fluid-model (TFM) within the Euler-Euler framework, and the discrete-element-method (DEM) or particle-in-cell (PIC) within the Euler-Lagrange framework [5, 7, 8]. These methods provide feasible numerical tools for simulating complex flow phenomenon involving a large amount of granular material, e.g., fluidized bed [9], blood cell flow [10], and microgel suspension [11].

Moreover, VANSE also contributes to underpin the widely-adopted Darcy-Brinkman-Stokes (DBS) approach within the micro-continuum framework, which has significantly advanced the multiscale modeling of flow behavior at representative-elementary-volume (REV) scale [12]. When coupled with a range of multiphysical processes (e.g., volume-of-fluid interface tracking methods, species transport equations, poroelasticity methodologies and crystal nucleation theories), the DBS framework has provided promising paths for addressing various challenges in porous flow systems, including mineral dissolution [13], coke combustion [14], matrix deformation [15] and capillary/viscous fracturing [16].

As a mesoscopic numerical tool that has made outstanding progress in modeling multiphase flow, the lattice Boltzmann method (LBM) recently has been extended to solve VANSE systems, due to its notable advantages in handling complex boundaries, ease of implementation and flexibility in parallel computing [17]. From a bottom-up approach, the so-called gray-LB model was proposed to simulate fluid behavior in the presence of sub-resolution solid effects, which modified the propagation step by introducing a partial bounce-back fraction (corresponding to the void fraction in VANSE) to mimic local fluid-solid interactions [18-20]. However, the numerically obtained fluid-solid force was viscosity-dependent and non-physical, in this case, the gray-LB model was incompatible with VANSE as it failed to accurately reproduce macroscale behaviors [21].

On the other hand, a series of numerical studies following the up-bottom concept to recover VANSE has made progress, facilitating the emergence of some mesoscopic fluid-solid models within the LBM framework. Notably, Guo et al. [22] pioneered a REV-scale LB model that recovered the generalized NSE (a simplified version of VANSE) for porous flows. Although this model is primarily effective for cases with a uniform void fraction field, it has been widely extended in various applicable scenarios, e.g., immiscible multiphase seepage [23], fluid flow through moving porous media [24], and frost growth on cold surfaces [25]. To the best of our knowledge, the prototype of the density-based LB scheme for the full form of VANSE was first proposed by Wang et al. [26] and later theoretically validated by Zhang et al [2], which incorporated a correction force for the recovered pressure term. However, this

correction force could induce significant non-physical pressure jumps and spurious currents in heterogeneous void fraction fields. Despite these shortcomings, this scheme has been used to develop TFM-LBMs for flow systems small gradients of void fraction [27, 28]. Alternatively, Höcker et al. [29] eliminated the non-physical pressure oscillation by manipulating the LB streaming step, thereby avoiding the need for force correction, and this approach was successfully implanted into DEM-LBM to model reactive particle-fluid flows [30]. Unfortunately, the recovered continuity equation and viscous term remained inconsistent with those in VANSE. Blais et al. [3] introduced a novel collision operator to accurately recover VANSE with a constructed correction term for deviatoric stress tensor. This treatment improved the stability of pressure calculations for very large void fraction gradients, but its solution diverges when the void fraction falls below 0.5. Subsequently, Bukreev et al. [4] redefined the zeroth moment of population distribution (i.e., the density equilibrium distribution) with locally-integral values of void fraction, thereby recovering VANSE with second-order convergence, while this algorithm still suffers from spurious currents at discontinuous distributions. Recently, Fu et al. [1] developed a pressure-based LB scheme decoupling pressure from density, which effectively reduced unwanted spurious currents and yielded second-order convergence in VANSE recovery. Although this scheme has been validated to have robust numerical performance for spatiotemporal void fraction field, the application of density evolution is still mainstream in current LB community, thus the density-based VANSE-LBM needs further improvement.

In this work, a novel multiple-relaxation-time lattice Boltzmann method for VANSE (MRTL-B-VANSE) is devised. Specifically, a provisional equation of state is introduced to decouple the void fraction from density by modifying the equilibrium distribution of the density-based LB scheme. Although this scheme still employs a correction force to address the inconsistency of the pressure gradient term, it avoids the need to discretize the void fraction gradient in force calculations. Additionally, inspired by the works of Li et. al [31, 32] and confirmed by Chapman-Enskog analysis, the MRT collision operator enables the reconstruction of a penalty source term in moment space, effectively eliminating the numerical errors of

viscous stress tensor in the recovered macroscopic momentum. Accordingly, this paper is structured as follows: Section 2 introduces the general form of VANSE, discusses the numerical errors and failure reasons in previous VANSE-LB models, and devises the specific framework of the consistent MRTLB-VANSE scheme; Section 3 conducts some numerical validations, including benchmarks against analytical solutions, spurious current testing, and convergence verification of VANSE for spatial and spatiotemporal void fraction fields; Section 4 concludes this paper and suggests the plans for future research; At last, Appendix A details the Chapman-Enskog analysis, confirming the devised scheme's consistency with VANSE; Appendix B additionally presents the second-order equilibrium distribution and the penalty source term within the MRT-VANSE framework; Appendix C gives three specific expressions of body force used for convergence verification.

2. Methodology

2.1. Volume-averaged Navier-Stokes equations

Historically, several versions of VANSE have been proposed based on different concepts of volume-averaging and approaches to solving fluid stress tensor, as thoroughly reviewed by Zhou et al.[5] In this paper, the formulation of model A (set II) is adopted without loss of generality, since it could be transformed into model B (set I) via some special treatments. The continuity and momentum equations of model A can be expressed as follows

$$\begin{aligned}\partial_t(\phi\rho) + \nabla \cdot (\phi\rho\mathbf{u}) &= 0, \\ \partial_t(\phi\rho\mathbf{u}) + \nabla \cdot (\phi\rho\mathbf{u}\mathbf{u}) &= -\phi\nabla p + \nabla \cdot (\phi\boldsymbol{\tau}) + \mathbf{F},\end{aligned}\tag{1}$$

where ϕ , ρ , p and \mathbf{u} are the void fraction, density, pressure and velocity of fluid; \mathbf{F} is the body force term containing the drag force for fluid-solid coupling and other external forces; $\boldsymbol{\tau}$ is the viscous stress tensor for Newtonian fluids

$$\boldsymbol{\tau} = \rho\nu\left((\nabla\mathbf{u}) + (\nabla\mathbf{u})^T - \frac{2}{3}(\nabla \cdot \mathbf{u})\mathbf{I}\right),\tag{2}$$

where ν is kinematic viscosity, and the last term of right hand cannot be omitted here since the divergence of velocity for VANSE is nonzero in a void fraction field.

2.2. Numerical error of BGK-LB method for VANSE

The LB scheme with the Bhatnagar-Gross-Krook (BGK) collision operator for recovering

VANSE was first theoretically devised by Wang et al.[26] and Zhang et al.[2], which evolves the local information of fluid mass via redefining the density distribution function in the discrete LB equation, expressed as

$$f_i(\mathbf{x} + \mathbf{e}_i \delta_t, t + \delta_t) = f_i(\mathbf{x}, t) - \tau_v (f_i(\mathbf{x}, t) - f_i^{eq}(\mathbf{x}, t)) + \delta_t \left(1 - \frac{\tau_v}{2}\right) F_i(\mathbf{x}, t), \quad (3)$$

where $f_i(\mathbf{x}, t)$ is the population distribution at the position \mathbf{x} and time t in the i -th discrete direction, $f_i(\mathbf{x} + \mathbf{e}_i \delta_t, t + \delta_t)$ is the post-collision distribution, and the equilibrium distribution f_i^{eq} is defined as

$$f_i^{eq}(\mathbf{x}, t) = \omega_i \phi \rho \left(1 + \frac{\mathbf{e}_i \cdot \mathbf{u}}{c_s^2} + \frac{(\mathbf{e}_i \cdot \mathbf{u})^2}{2c_s^4} - \frac{\mathbf{u} \cdot \mathbf{u}}{2c_s^2}\right), \quad (4)$$

where the rescaling of density ρ into $\phi \rho$ allows the LB equation to be correlated from NSE to VANSE, and the lattice sound speed is given by $c_s = c/\sqrt{3}$, bridging the relaxation factor τ_v with the shear viscosity ν , i.e., $\tau_v^{-1} = \nu/c_s^2 \delta_t + 0.5$. The D2Q9 lattice stencil with a constant lattice speed $c = \delta_x/\delta_t = 1$ is employed in this paper, and it can straightforwardly be extended to 3D and other lattices. The discrete lattice velocity \mathbf{e}_i and the corresponding weight coefficients ω_i are provided as

$$\mathbf{e}_i = \begin{cases} (0, 0), & \omega_0 = 4/9 \\ (\cos[(i-1)\pi/2], \sin[(i-1)\pi/2])c, & \omega_{1-4} = 1/9 \\ (\cos[(2i-9)\pi/4], \sin[(2i-9)\pi/4])\sqrt{2}c, & \omega_{5-8} = 1/36 \end{cases}. \quad (5)$$

Furthermore, the force term F_i that takes account of an additional term $\mathbf{F}^p = \rho c_s^2 \nabla \phi$ responsible for correcting the pressure gradient in VANSE, as well as the external body force \mathbf{F}^B , is given with the scheme of Guo et al.[33]

$$F_i(\mathbf{x}, t) = \omega_i \left(\frac{\mathbf{e}_i - \mathbf{u}}{c_s^2} + \frac{\mathbf{e}_i \cdot \mathbf{u}}{c_s^4} \mathbf{e}_i \right) \cdot (\mathbf{F}^p + \mathbf{F}^B). \quad (6)$$

Then, the macroscopic fluid density, velocity, and pressure can be obtained via the moments of the distribution function

$$\rho = \sum_i f_i / \phi, \quad \mathbf{u} = \left(\sum_i \mathbf{e}_i f_i + \frac{\delta_t}{2} (\mathbf{F}^p + \mathbf{F}^B) \right) / \sum_i f_i, \quad p = \rho c_s^2 \quad (7)$$

Accordingly, through the third-order Chapman-Enskog analysis of Eq. (3), the following macroscopic equations can be recovered when the external body force \mathbf{F}^B is ignored [34]

$$\partial_t(\phi \rho) + \nabla \cdot (\phi \rho \mathbf{u}) = 0, \quad (8)$$

$$\partial_t(\phi\rho\mathbf{u}) + \nabla \cdot (\phi\rho\mathbf{u}\mathbf{u}) = -\nabla(\phi p) + \mathbf{F}^p + \nu\nabla \cdot (\phi\boldsymbol{\tau}) + \frac{\delta_t^2}{12} \nabla \cdot \nabla \mathbf{F}^p. \quad (9)$$

The last term on the right side of Eq. (9) is the high-order error that inevitably occurs when the pressure correction is applied in force term. Moreover, it should be noted that in discrete space, the value of “ $-\nabla(\phi p) + \mathbf{F}^p$ ” is not exactly equal to the correct pressure term “ $-\phi\nabla p$ ” in Eq. (1) as continuous derivatives. In this paper, the isotropic finite difference stencil is used, so that the gradient operator for a variable ψ is discretely evaluated as follows[35]

$$\partial_\alpha \psi(\mathbf{x}) = \frac{1}{c_s^2 \delta_t} \sum_i \omega_i \psi(\mathbf{x} + \mathbf{e}_i \delta_t) \mathbf{e}_{i\alpha}. \quad (10)$$

Through Taylor expansion for this difference stencil in D2Q9 space, the correction force and its error can be deduced

$$\tilde{\mathbf{F}}^p = \mathbf{F}^p + \frac{\delta_t^2}{6} \nabla(\nabla \cdot \mathbf{F}^p) + \dots \quad (11)$$

Assuming that the influence of weak compressibility of LB scheme is negligible, the total numerical error below the fourth-order combining Eq. (9) and Eq. (11) is given by

$$F^{error} = \frac{\delta_t^2}{12} \nabla \cdot \nabla \mathbf{F}^p + \frac{\delta_t^2}{6} \nabla(\nabla \cdot \mathbf{F}^p) = \frac{\rho}{12} \nabla(\nabla^2 \phi). \quad (12)$$

This error cannot be ignored when ϕ is distributed with large gradients, as it could lead to non-physical acceleration in flow field, resulting in spurious currents that exceed the low Mach number limit of LBM. This is the primary issue of numerical instability and inconsistency of the BGKLB-VANSE scheme for spatiotemporal volume fraction field.

2.3. Consistent MRT-LB method for VANSE

The consistent LB scheme presented in this section still uses the forcing term for pressure correction towards VANSE. Fundamentally speaking, the use of $\mathbf{F}^p = \rho c_s^2 \nabla \phi$ in Eq. (6) originates from the definition of $\phi\rho$ in Eq. (4), which recovers the equation of state $p^{EOS} = \phi\rho c_s^2$ within the inconsistent pressure gradient term of Eq. (9). To remedy this issue, a provisional equation of state $p_0^{EOS} = \kappa\rho c_s^2$ is adopted to replace ∇p^{EOS} with ∇p_0^{EOS} in Eq. (9). Meanwhile, the pressure correction force is readjusted into

$$\mathbf{F}^p = \nabla(\kappa\rho c_s^2) - \phi\nabla(\rho c_s^2) = (\kappa - \phi)c_s^2 \nabla\rho \quad (13)$$

where ϕ and ρ are decoupled in gradient operator, $0 \leq \kappa \leq 1$ is a constant suggested to choose close to the minimum void fraction of the whole domain. Obviously, this force term is

independent of $\nabla\phi$, and its value converges to zero after a certain calculation step for incompressible flows with constant density. Even for multiphase flow, the treatment of dissipative interfaces in LBM results in density typically varying between several lattice nodes, instead of intermittent distribution. Hence, this setup effectively avoids non-physical oscillations at the discontinuities of void fraction field.

In order to yield the provisional equation of state mentioned above, the equilibrium density function built from the 3d-order Hermite expansion of Maxwellian distribution is adopted here [31, 36, 37]

$$f_i^{eq}(\mathbf{x}, t) = \begin{cases} \phi\rho - \sum_{i \neq 0} \omega_i \kappa\rho - \omega_0 \phi\rho \frac{\mathbf{u} \cdot \mathbf{u}}{2c_s^2}, & i = 0 \\ \omega_i \left(\kappa\rho + \phi\rho \left(\frac{\mathbf{e}_i \cdot \mathbf{u}}{c_s^2} \left(1 + \frac{1}{2} (X-1) \left(\frac{\mathbf{e}_i^2}{c_s^2} - 4 \right) \right) + \frac{(\mathbf{e}_i \cdot \mathbf{u})^2}{2c_s^4} - \frac{\mathbf{u} \cdot \mathbf{u}}{2c_s^2} \right) \right), & i = 1 \sim 8 \end{cases} \quad (14)$$

where $X = P_0^{EOS} / P^{EOS} = \kappa / \phi$, and its 0th- to 3rd-order velocity moments can be calculated

$$\begin{aligned} \sum_i f_i^{eq} &= \phi\rho, \\ \sum_i f_i^{eq} \mathbf{e}_{i\alpha} &= \phi\rho u_\alpha, \\ \sum_i f_i^{eq} \mathbf{e}_{i\alpha} \mathbf{e}_{i\beta} &= \phi\rho u_\alpha u_\beta + \kappa\rho c_s^2 \delta_{\alpha\beta}, \\ \sum_i f_i^{eq} \mathbf{e}_{i\alpha} \mathbf{e}_{i\beta} \mathbf{e}_{i\gamma} &= \begin{cases} \phi\rho c_s^2 (u_\gamma \delta_{\alpha\beta} + u_\beta \delta_{\alpha\gamma} + u_\alpha \delta_{\beta\gamma}), & \text{if } i = j = k, \\ \kappa\rho c_s^2 (u_\gamma \delta_{\alpha\beta} + u_\beta \delta_{\alpha\gamma} + u_\alpha \delta_{\beta\gamma}), & \text{otherwise,} \end{cases} \end{aligned} \quad (15)$$

where δ is the Kronecker delta with two indices. Evidently, the zeroth and first-order moments are identic with the BGK-LB-VANSE scheme given by Zhang et al.[2], so the macro parameters are still calculated by Eq. (7), meanwhile, the pressure term in the second-order moment is successfully modified. However, in the third-order moment, the introduction of the provisional equation of state produces bias that brings numerical errors in the recovered viscous stress tensor, thereby making the Galilean invariance of the momentum equations violated[38, 39]. Consequently, motivated by the pioneer work of Li et al.[31], we employ the multiple-relaxation-time (MRT) collision operator in this paper to eliminate this unwanted error via adding a source term in moment space. This strategy has also been utilized to treat such issue in color-gradient and free-energy multiphase LB models[32, 37, 40, 41]. Besides, the use of MRT scheme for VANSE has more robust numerical performance compared with BGK, which

will be demonstrate in the following.

Multiplying Eq. (3) with the transformation matrix \mathbf{M} cf. Appendix A, the MRT-LB evolution equation for VANSE is expressed as

$$\mathbf{m}^+ = \mathbf{m} - \Gamma(\mathbf{m} - \mathbf{m}^{eq}) + \delta_t \left(\mathbf{I} - \frac{\Gamma}{2} \right) (\mathbf{S} + \mathbf{C}), \quad (16)$$

where the population distribution in moment space is mapped by $m_i = \sum_j \mathbf{M}_{ij} f_j$, written as

$$\mathbf{m} = \mathbf{M}\mathbf{f} = (m_0, m_1, \dots, m_8)^\top = (\phi\rho, e, \varepsilon, j_x, q_x, j_y, q_y, p_{xx}, p_{xy})^\top, \quad (17)$$

in which e is the energy mode, ε is related to the energy square, (q_x, q_y) are the energy flux, $(j_x, j_y) = (\phi\rho u_x - \delta_t F_x / 2, \phi\rho u_y - \delta_t F_y / 2)$ are the components of momentum, and (p_{xx}, p_{xy}) correspond to the diagonal and off-diagonal components of the stress tensors[42].

Based on Eq. (14), the equilibrium moment $m_i^{eq} = \sum_{j,k} \mathbf{M}_{ij} f_j^{eq}$ can be explicitly given by

$$\mathbf{m}^{eq} = \mathbf{M}\mathbf{f}^{eq} = (m_0^{eq}, m_1^{eq}, \dots, m_8^{eq})^\top = \phi\rho \left(1, -4 + 3\mathbf{u}^2 + 2X, 4 - 3\mathbf{u}^2 - 3X, u_x, (X-2)u_x, u_y, (X-2)u_y, u_x^2 - u_y^2, u_x u_y \right)^\top, \quad (18)$$

Similarly, the force moment $S_i = \sum_{j,k} \mathbf{M}_{ij} F_j$ can be derived from Eq. (6), expressed as

$$\mathbf{S} = \mathbf{M}\mathbf{F} = (S_0, S_1, \dots, S_8)^\top = \left(0, 6\mathbf{u} \cdot \mathbf{F}, -6\mathbf{u} \cdot \mathbf{F}, F_x, -F_x, F_y, -F_y, 2(u_x F_x - u_y F_y), u_x F_y + u_y F_x \right)^\top. \quad (19)$$

Moreover, \mathbf{m}^+ is the moment distribution that required to project back to the discrete space for streaming step, i.e., $f_i(\mathbf{x} + \mathbf{e}_i \delta_t, t + \delta_t) = f_i^+(\mathbf{x}, t)$, therein $\mathbf{f}^+ = \mathbf{M}^{-1} \mathbf{m}^+$ and \mathbf{M}^{-1} is the inverse matrix of \mathbf{M} cf. Appendix A. \mathbf{I} is the unit matrix; $\Gamma = \text{diag}(\tau_c, \tau_e, \tau_e, \tau_e, \tau_q, \tau_c, \tau_q, \tau_v, \tau_v)$ is the non-negative relaxation matrix, therein $\tau_c = 1$ is chosen for density and momentum conservation, $\tau_e = 1.2, \tau_q = 1.4$ are chosen for numerical stability requirements, and τ_e is related to the bulk viscosity ν_e , i.e., $\tau_e = (\nu_e / c_s^2 \delta_t + 0.5)^{-1}$; $\mathbf{C} = (0, C_a, 0, 0, 0, 0, 0, C_b, C_c)^\top$ is the penalty source term for viscous stress correction composed by

$$\begin{aligned} C_a &= -\kappa \left(\partial_x (\rho u_x) + \partial_y (\rho u_y) \right) + 2(\kappa - \phi) \rho (\partial_x u_x + \partial_y u_y) \\ &\quad + (3 - 2X) \left(\partial_x (\phi \rho u_x) + \partial_y (\phi \rho u_y) \right) - 2X \rho \partial_t \phi, \\ C_b &= -\kappa \left(\partial_x (\rho u_x) - \partial_y (\rho u_y) \right) + \frac{2}{3} (\kappa - \phi) \rho (\partial_x u_x - \partial_y u_y) \\ &\quad + \left(\partial_x (\phi \rho u_x) - \partial_y (\phi \rho u_y) \right), \\ C_c &= \frac{1}{3} (\kappa - \phi) \rho (\partial_x u_y + \partial_y u_x), \end{aligned} \quad (20)$$

where the spatial derivative $\nabla = (\partial_x, \partial_y)$ is calculated by Eq. (10), the time derivative is

evaluated by the first-order Euler scheme, i.e., $\partial_t \phi = (\phi(\mathbf{x}, t + \delta_t) - \phi(\mathbf{x}, t)) / \delta_t$.

Based on the above, this designed MRT-LB scheme can exactly recover the consistent VANSE, which is confirmed by Chapman-Enskog analysis cf. Appendix A. Notably, if we use $\mathbf{F}^p = (\kappa - 1)c_s^2 \nabla \rho$ for pressure correction instead of Eq. (13) and change the term “ $\kappa - \phi$ ” to “ $\kappa - 1$ ” in the penalty source term of Eq. (20), the model B (set I) version of VANSE can be recovered with correct pressure gradient term and viscous stress tensor. Additionally, in framework of the MRT scheme mentioned above, we also provide the scheme of widely-adopted 2nd-order equilibrium distribution and its penalty source term, cf. Appendix B. They make the similar effects in Chapman-Enskog analysis as derived in Appendix A to recover VANSE, without losing the consistency and accuracy. However, it is observed that the gradient calculation in Eq. (20) is reduced compared with Eq. (B3), which is more advantageous for computational efficiency and numerical convergence. Thus, we still use the MRT-LB-VANSE scheme with the 3rd-order equilibrium distribution henceforth to further validate.

3. Numerical validation

In this section, the physical correctness of the established MRT-LB-VANSE is validated against analytical solutions of several typical benchmark scenarios, and its convergence accuracy has been tested by the method of manufactured solutions (MMS). The computational domain in all test cases are discretized by the D2Q9 lattice space with periodic boundaries unless otherwise specified, and the fluid density ρ is initialized as 1.0, the kinematic viscosity ν is 0.1, and the constant κ is chosen as 0.5.

3.1 Uniform porous flow

Accurately describing the flow behavior within a homogeneous substrate with uniform porosity field is a basic capability of VANSE. Neglecting the nonlinear Forchheimer force that characterizes inertial effects, and incorporating the external force G_x and the linear Darcy resistance $\phi \nu u k_0^{-1}$ induced by fluid-solid interactions within the body force term in Eq. (6), i.e., $F_x^B = \phi(G_x - \phi \nu u k_0^{-1})$, VANSE can be reduced to the Darcy-Brinkman equation governing flow at representative elementary volume (REV) scale[22, 23, 43]

$$\nu \frac{\partial^2 u}{\partial y^2} - \frac{\phi \nu}{k_0} u + G_x = 0, \quad (21)$$

where u is the real velocity in y -section, k_0 is the medium permeability that characterized by the dimensionless Darcy number $Da = k_0 / H^2$ ranging from 10^{-6} to 10^{-2} as ϕ varies from 0.1 to 0.5. Under different boundary conditions, the velocity profiles of porous Poiseuille flow (I) and Couette flow (II) can be analytically solved from Eq. (21) [22, 29]

$$(I) \quad G_x = 10^{-6}, \quad u_{y=H} = 0, \quad u_{y=0} = 0, \quad u(y) = \frac{G_x k_0}{\phi \nu} \left(1 - \frac{\cosh(\sqrt{\phi / k_0} (y - H/2))}{\cosh(\sqrt{\phi / k_0} H/2)} \right), \quad (22)$$

$$(II) \quad G_x = 0, \quad u_{y=0} = 0, \quad u_{y=H} = 10^{-3}, \quad u(y) = u_{y=H} \frac{\sinh(\sqrt{\phi / k_0} y)}{\sinh(\sqrt{\phi / k_0} H)}.$$

In LB coding, the no-slip boundary condition at the solid wall and the velocity condition in Couette flow are respectively implemented by the half bounce-back and the non-equilibrium extrapolation scheme[44]. As illustrated in Fig. 1 (a) and (b), it is observed that the simulation results are in good agreements with their analytical solutions for different values of Da or ϕ , which demonstrates MRTLB-VANSE is capable of reproducing the REV-scale flow at various volume-averaging levels.

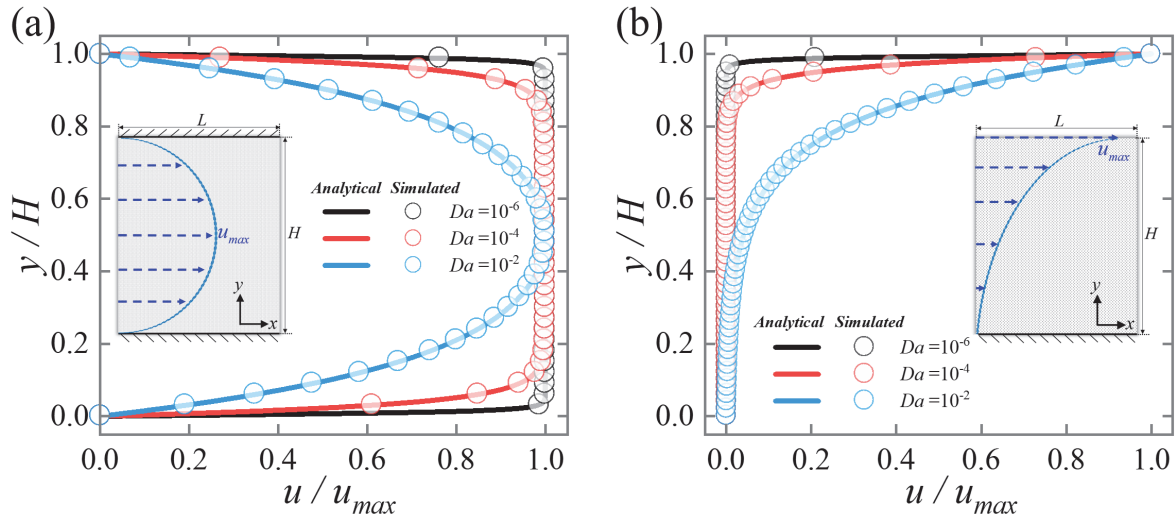


Fig. 1. Normalized velocity profiles and the illustrations of simulation scenarios for the porous Poiseuille flow (a), Couette flow (b) within a uniform porosity field, with the computational domain size set as $L \times H = 100 \times 50$.

3.2 Nonuniform particle flow

To validate the pressure term in VANSE, a simplistic scenario of 1-D nonuniform particle flow within a spatially and temporally fluctuating void fraction field is considered [29, 41]. Given the numerical error of Eq. (12) becomes nonzero in the presence of void fraction

gradients, this test serves as evidence for the accuracy of the improved VANSE scheme. By artificially constructing a specific fluid-solid drag law as well as the void fraction function, the velocity distribution can be analytically solved, which are expressed as follows

$$\begin{aligned}\phi(x,t) &= 1 + a \left(\sin \frac{2\pi}{L} (x - u_s t) - 1 \right), \\ F_x^B(x,t) &= \phi (G_x - \phi(1-\phi)(u - u_s)), \\ u(x,t) &= u_s + \frac{G_x}{a\phi}\end{aligned}\quad (23)$$

where the external force is fixed at $G_x = 10^{-6}$, a and u_s are constants that control the amplitude of void fraction fluctuation in space and time, respectively.

Two verification cases are displayed in the schematic diagrams of Fig. 2 (a) and (b): one steady-state ($u_s = 0$) and one transient ($a = 0.45$). As clearly demonstrated, the simulate results align with the analytical solution of Eq. (23) under fluctuations of different amplitudes (i.e., $a = 0.15 \sim 0.45$, $u_s = 10^{-5} \sim 10^{-3}$), confirming that the pressure correction scheme in MRTLB-VANSE is consistent and reliable.

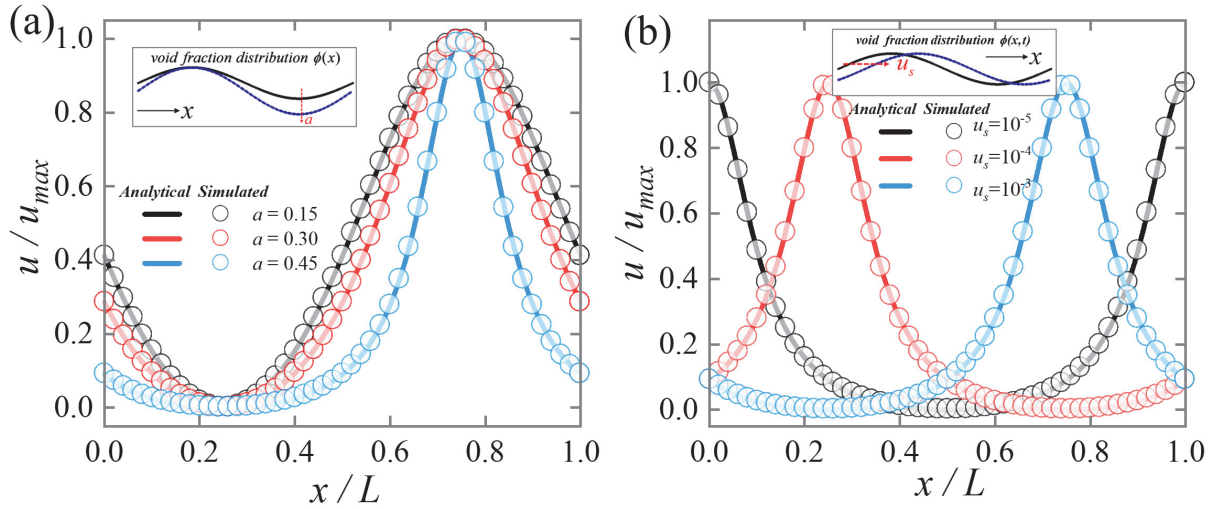


Fig. 2. Normalized velocity profiles of the 1-D nonuniform particle flow and schematic diagrams of the void fraction distribution for the steady-state case (a), the transient case at $t = 5 \times 10^6$ (b), with the computational domain set as $L \times H = 100 \times 5$.

3.3 Flow in discontinuous field

In an initially quiescent flow field, the velocity distribution theoretically remains zero under no external driving force and inlet flow. However, the BGKLB-VANSE scheme suffers from significant spurious velocities in the presence of void fraction gradients, primarily caused

by the numerical error of the discretized correction force, i.e., Eq. (12), which lead to non-physical acceleration for fluid. To evaluate the ability of MRTLB-VANSE to relieve this issue, a discontinuous void fraction field is configured to conduct a no-flow verification

$$\phi(x, y) = \begin{cases} \phi_0, & \forall (x, y) \in \Omega_s = [0.4L, 0.6L] \times [0.4H, 0.6H] \\ 1, & \forall (x, y) \in \Omega / \Omega_s \end{cases} \quad (24)$$

where the 2-D computational domain Ω is set with the size $L \times H = 100 \times 100$, ϕ_0 is a constant less than 1, thus forming a discontinuous field.

As shown in Fig. 3, the maximum spurious velocities simulated by MRTLB-VANSE for domains with different ϕ_0 are compared with the previous density-based schemes, Zhang et al.[2], Bukreev et al.[4] and Blais et al.[3]. It is evident that although Bukreev et al. provided some improvement and Blais et al. reduced the spurious velocity a lot, their schemes cannot suit for high void fraction gradients at $\phi_0 \leq 0.3$. Exceptionally, MRTLB-VANSE demonstrates relatively low spurious velocities in the no-flow tests across different discontinuous cases. This good numerical performance can be attributed not only to the new corrected force of Eq. (13) but also, more significantly, owing to the redefined density equilibrium distribution of Eq. (14), which means the density distribution for $i \neq 0$ are no longer dependent on local void fraction, ensuring that the initialized $f_{i \neq 0}$ still preserve isotropy within a non-uniform void fraction field after the streaming step. Consequently, the first moment of the density distribution approximates zero, thereby producing the very low spurious velocities. Recently, Fu et al. [1] even achieved exactly-zero spurious velocities in their no-flow tests, where the influence of weak compressibility on flow field can be avoided by employing the pressure-based equilibrium distribution. Although we cannot entirely overcome the generation of spurious velocities due to the natural limitations of weak compressibility in density-based LB method, the designed MRTLB scheme has significantly improved the numerical performance of VANSE-LB model.

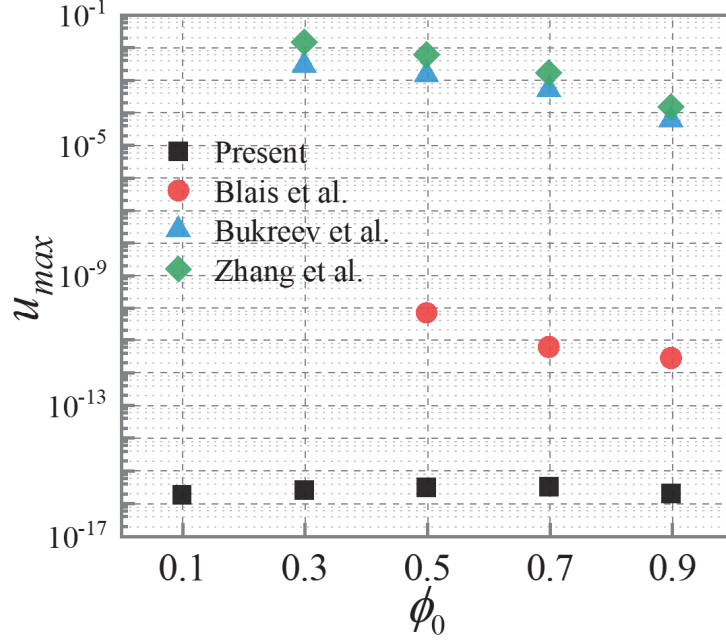


Fig. 3. Maximum spurious velocities of within the computational domain in the no-flow test

Furthermore, the discontinuous flow is tested by applying a external force $G_x = 10^{-6}$ towards the computational domain Ω described in Eq. (24). First, the block area of Ω_s is set as solid with $\phi_0 = 0$, and the flow field under this impermeable condition is served as a reference case as shown in Fig. 4(a). Subsequently, ϕ_0 is adjusted to 0.5 and a high Darcy resistance ($Da = 10^{-6}$) is exerted in Ω_s to hinder fluid flow. Ideally, the flow fields obtained from the two geometric configurations of Ω_s ought to be similar. As exhibited in Fig. 4, the velocity distributions simulated by the schemes of Zhang et al. and Bukreev et al. deviate from the reference case due to unacceptable spurious velocities; Blais et al.'s scheme provides consistent results, but unfortunately it fails to converge when $\phi_0 < 0.5$; Both Fu et al.'s and the MRTLB-VASNE schemes successfully produce results for $\phi_0 < 0.5$, nonetheless, Fig. 4(c) shows a slight velocity fluctuations for $\phi_0 = 0.2$ due to the presence of large pressure gradient at the free-permeable interface there; and obviously, the MRTLB-VANSE scheme performs well at $\phi_0 = 0.5, 0.2$ and produces velocity fields consistent with the reference case, which strongly confirms its numerical robustness.

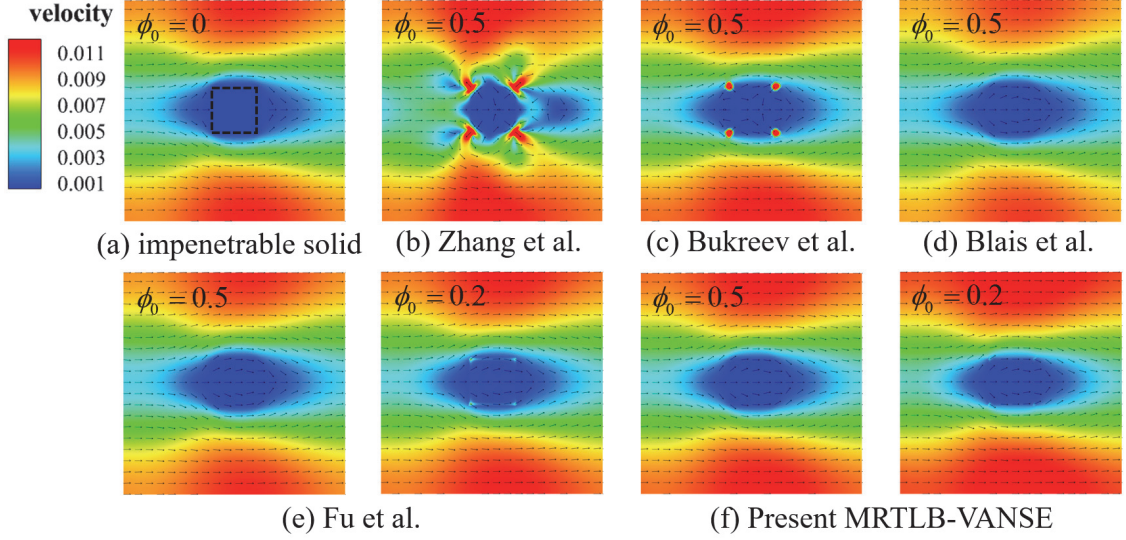


Fig. 4. The velocity distribution of forced discontinuous flow, where the domain center is arranged as a block with the constant void fraction, as indicate by the black dashed line in (a).

3.4 Convergence test

The method of manufactured solutions (MMS) is a straightforward approach to constructing analytical solutions for partial differential equations [45, 46], which has been widely adopted as a standard procedure to test the convergence accuracy of a LB scheme for solving VANSE [1, 3, 4]. First, the settings of velocity $\tilde{\mathbf{u}}$ and void fraction $\tilde{\phi}$ are manufactured to meet the continuity equation in Eq. (1), and then a body force is further applied in Eq. (6) to satisfy momentum conservation

$$\mathbf{F}^b(\tilde{\mathbf{u}}, \tilde{\phi}) = \partial_i (\tilde{\phi} \rho \tilde{\mathbf{u}}) + \nabla \cdot (\tilde{\phi} \rho \tilde{\mathbf{u}} \tilde{\mathbf{u}}) + \tilde{\phi} \nabla p - \nu \nabla \cdot \left(\tilde{\phi} \rho \left((\nabla \tilde{\mathbf{u}}) + (\nabla \tilde{\mathbf{u}})^T - \frac{2}{3} (\nabla \cdot \tilde{\mathbf{u}}) \mathbf{I} \right) \right) \quad (25)$$

which includes all term of the momentum equation and makes the manufactured settings become the theoretical exact solution for VANSE. To monitor the numerical results of MRTLB-VANSE, the Euclidean norm of the relative velocity is introduced

$$E_u = \sqrt{\frac{\sum_i^N |\mathbf{u}_i - \tilde{\mathbf{u}}_i|^2}{\sum_i^N |\tilde{\mathbf{u}}_i|^2}} \quad (26)$$

where \mathbf{u}_i and $\tilde{\mathbf{u}}_i$ denote the numerical and manufactured values, respectively, $N = L \times H$ is the total number of lattice nodes. Due to the use of periodic boundary conditions towards the computational domain, the error norm is only recorded as an asymptotically stable value after sufficiently long simulation steps. The macroscopic size of the test domain in this section is fixed as 1×1 , with the same number of lattice nodes in x and y directions (i.e., $L = H = n$), and

the unit length per lattice is denoted as $\Delta x = 1/n$.

Taking different cases of void fraction with spatial and spatiotemporal variations into account, three manufactured settings are designed as follows

$$(I) \quad \begin{aligned} \tilde{\phi} &= a + b \sin(\pi x^*) \sin(\pi y^*), \\ \tilde{\mathbf{u}} &= u_s \Delta x \begin{bmatrix} -\sin^2(\pi x^*) \sin(\pi y^*) \cos(\pi y^*) \\ \sin^2(\pi y^*) \sin(\pi x^*) \cos(\pi x^*) \end{bmatrix} \end{aligned} \quad (27)$$

$$(II) \quad \begin{aligned} \tilde{\phi} &= a \exp(-b \sin(\pi x^*) \sin(\pi y^*)) \\ \tilde{\mathbf{u}} &= u_s \Delta x \exp(b \sin(\pi x^*) \sin(\pi y^*)) \begin{bmatrix} 1 \\ 1 \end{bmatrix} \end{aligned} \quad (28)$$

$$(III) \quad \begin{aligned} \tilde{\phi} &= a + b \sin(\pi x_t^*) \sin(\pi y_t^*) \\ \tilde{\mathbf{u}} &= u_s \Delta x \left(\frac{1}{\tilde{\phi}} - 2 \right) \begin{bmatrix} 1 \\ 1 \end{bmatrix} \end{aligned} \quad (29)$$

where a, b are constants responsible for the spatial distribution of void fraction, u_s is the reference velocity, and the coordinates are given in lattice units

$$\begin{aligned} x^* &= \frac{2x - n + 1}{n}, \quad y^* = \frac{2y - n + 1}{n} \\ x_t^* &= \frac{2x - n + 1}{n} + \frac{4u_s t}{n^2}, \quad y_t^* = \frac{2y - n + 1}{n} + \frac{4u_s t}{n^2} \end{aligned} \quad (30)$$

Then, substituting these manufactured continuous functions into Eq. (25), the MMS body force can be obtained through some derivative operations, as detailed in Appendix C. Note that since the density is initialized as a constant value, the pressure gradient term in the MMS body force is ignored, while the pressure correction force of Eq. (13) still takes effects in simulation.

The void fraction and steady-state velocity distributions of two stationary cases I and II are shown in Figs. 5 and 7, respectively, where u_s is both fixed at 0.8. Their void fraction fields only vary in space, and the difference between them is that the velocity field of case II is non-divergence-free, resulting in all terms of viscous stress tensor in Eq. (25) are non-zero. As presented in Figs. 6 and 8, it is observed that all slopes of the fitted lines are very close to 2, i.e., the simulated velocity errors E_u exhibit complete second-order convergence with the lattice spacing Δx . These results demonstrate that MRTLB-VANSE is validly without loss of accuracy for both divergence-free and non-divergence-free flows at different kinematic viscosities ν and large void fraction gradients.

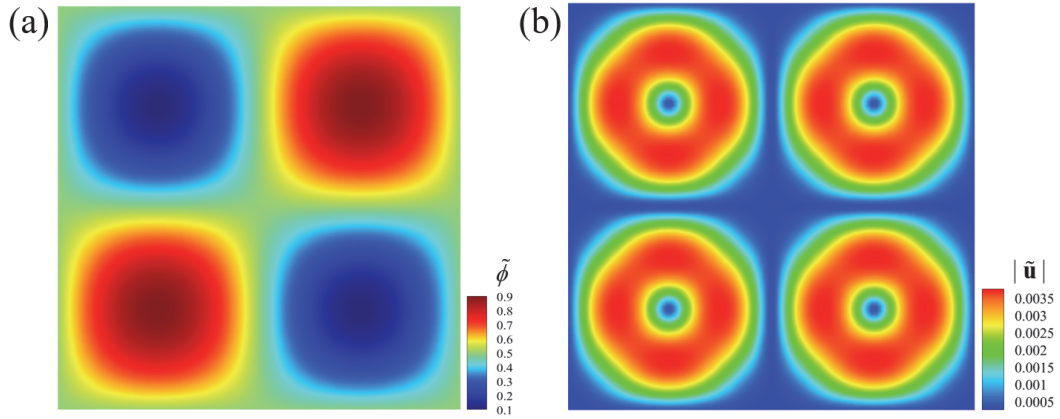


Fig. 5. A demo distributions of void fraction (a) and velocity (b) for case I with $a=0.5, b=0.4$, $n=100$, where the flow field is divergence-free.

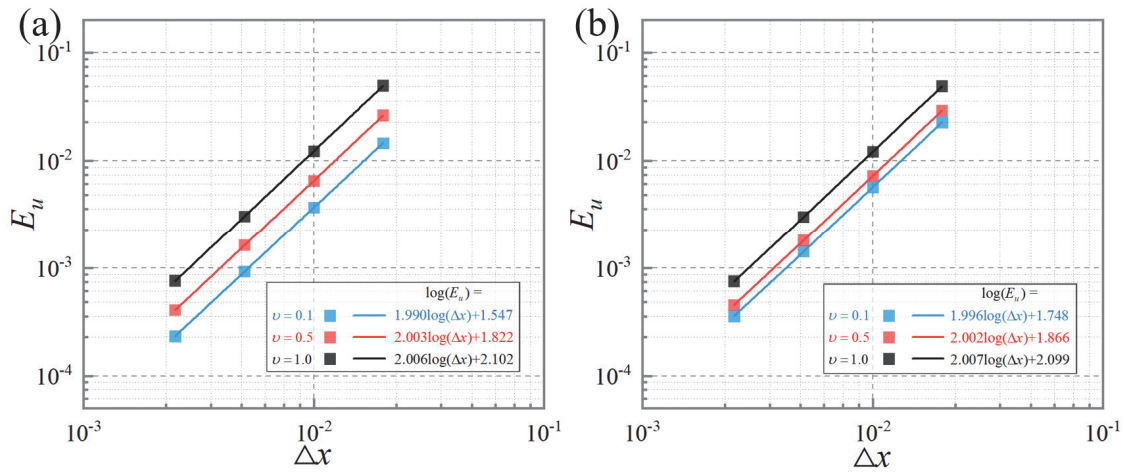


Fig. 6. Euclidean norm of velocity error as a function of lattice spacing for case I with two void fraction gradients: $a=0.5, b=0.4$ (a) and $a=0.5, b=0.49$ (b).

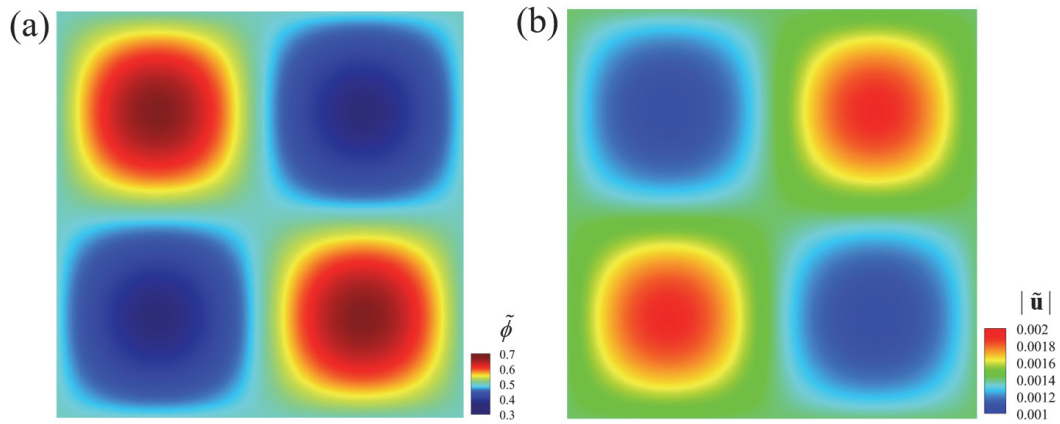


Fig. 7. A demo distributions of void fraction (a) and velocity (b) for case II with $a=0.5, b=0.3$, $n=100$, where the flow field is non-divergence-free.

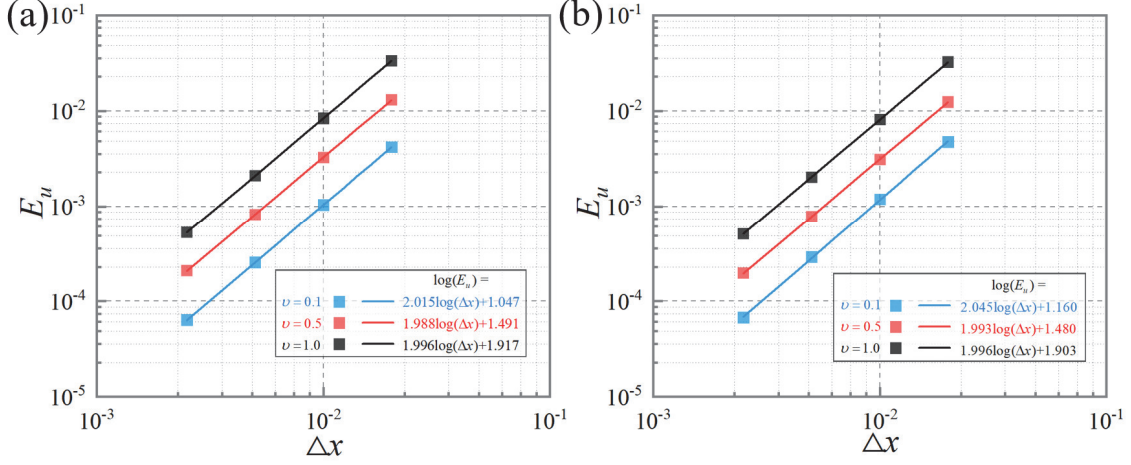


Fig. 8. Euclidean norm of velocity error as a function of lattice spacing for case II with two void fraction gradients: $a=0.5, b=0.3$ (a) and $a=0.5, b=0.5$ (b).

To further validate the accuracy of MRTLB-VANSE for full form of VANSE, the most complex transient case III is conducted with time-varying void fraction field. As displayed in Fig. 8, the manufactured void fraction and velocity field is movable in x and y directions with a period $T = n^2 / |4u_s|$, in which u_s is fixed at 0.08. In this case, the pressure-based method of Fu et al. is additionally recalled for comparison. In Fig. 9, it is observed that MRTLB-VANSE exhibits almost second-order convergence under different viscosities and void fraction gradients, meanwhile, its error norms show lower absolute values. Although Fu et al.'s method satisfies the second-order convergence at low viscosity ($\nu = 0.1$), it gradually loses accuracy at high viscosities ($\nu = 1.0$) due to the inherent instability of the SRT collision operator for relaxation times less than 0.5 [17]. This issue can be effectively eliminated by the MRT collision operator, which endows MRTLB-VANSE with better numerical performance.

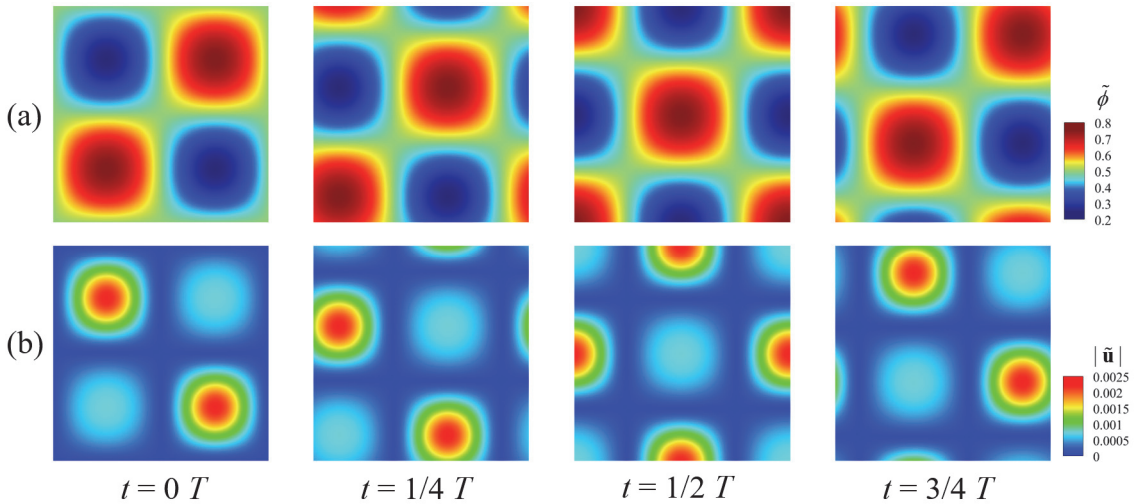


Fig. 8. A demo spatiotemporal distributions of void fraction (a) and velocity (b) for case III with

$a=0.5, b=0.25, n=100$, where the flow field is non-divergence-free.

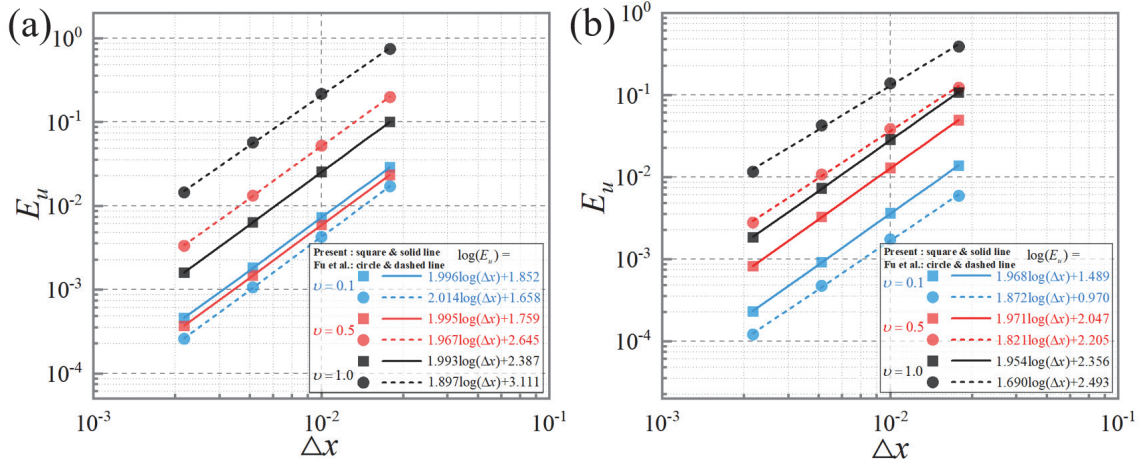


Fig. 9. Euclidean norm of velocity error as a function of lattice spacing for case III with two void fraction gradients: (a) $a=0.5, b=0.25$, (b) $a=0.5, b=0.45$, where the square samples and solid lines are results of MRTL-B-VANSE, and the circle samples and dashed lines are obtained by the method of Fu et al.

4. Conclusions

In this paper, a lattice Boltzmann method based on the MRT collision operator is developed to asymptotically solve VANSE. By adjusting the density equilibrium distribution, a provisional equation of state is incorporated to decouple the void fraction from density. On one hand, this decoupling not only eliminates the need to compute void fraction gradients in the pressure correction force, but also mitigates the force interference on flow field by introducing a numerical constant, thereby preventing non-physical oscillations caused by discretization errors at discontinuous distributions of void fraction. On the other hand, this decoupling ensures the population distributions remain isotropic when they stream in lattice space, which effectively suppresses spurious velocities calculated from their first-order moments. Moreover, the Galilean invariance of the recovered VANSE is guaranteed by applying a penalty source term in moment space to eliminate unwanted numerical errors of the viscous stress term.

This novel method is exactly confirmed by Chapman-Enskog analysis, and detailed numerical experiments are conducted to validate its effectiveness for VANSE, including analytical benchmarks (REV-scale porous flows, 1-D particle flow), no-flow tests in discontinuous void fraction fields, and the convergence validation through the method of manufactured solutions. These results demonstrate that the proposed method is capable of

recovering VANSE consistently with second-order accuracy, and suitable for void fraction fields with large gradients and spatiotemporal distributions. In comparison with previous methods, it shows satisfactory numerical performance, significantly advancing the applicability of the density-based VANS-LB schemes.

In future, extending this method to 3-D is straightforward, and given the inherent parallelizability and computational efficiency of LBM, it is promising to improve the reliability of industrial models related to VANSE. Furthermore, coupling concentration fields, temperature fields, immiscible multiphase models (color-gradient model, pseudo-potential model, phase-field model), and miscible fluid-solid models (TFM, DEM), a series of mesoscopic methods with engineering application potential can be developed to simulate complex liquid-gas-solid processes.

Acknowledgements

This research is funded by the National Key R&D Program of China (No. 2019YFA0708704).

Appendix A. Chapman-Enskog analysis

In this appendix, the Chapman-Enskog expansion is derived in detail to demonstrate that the established MRT-LB scheme can recover the consistent VANSE.

First, the 9×9 orthogonal matrix and its inverse matrix are presented

$$\mathbf{M} = \begin{pmatrix} 1 & 1 & 1 & 1 & 1 & 1 & 1 & 1 & 1 \\ -4 & -1 & -1 & -1 & -1 & 2 & 2 & 2 & 2 \\ 4 & -2 & -2 & -2 & -2 & 1 & 1 & 1 & 1 \\ 0 & 1 & 0 & -1 & 0 & 1 & -1 & -1 & 1 \\ 0 & -2 & 0 & 2 & 0 & 1 & -1 & -1 & 1 \\ 0 & 0 & 1 & 0 & -1 & 1 & 1 & -1 & -1 \\ 0 & 0 & -2 & 0 & 2 & 1 & 1 & -1 & -1 \\ 0 & 1 & -1 & 1 & -1 & 0 & 0 & 0 & 0 \\ 0 & 0 & 0 & 0 & 0 & 1 & -1 & 1 & -1 \end{pmatrix}, \mathbf{M}^{-1} = \frac{1}{36} \begin{pmatrix} 4 & -4 & 4 & 0 & 0 & 0 & 0 & 0 & 0 \\ 4 & -1 & -2 & 6 & -6 & 0 & 0 & 9 & 0 \\ 4 & -1 & -2 & 0 & 0 & 6 & -6 & -9 & 0 \\ 4 & -1 & -2 & -6 & 6 & 0 & 0 & 9 & 0 \\ 4 & -1 & -2 & 0 & 0 & -6 & 6 & -9 & 0 \\ 4 & 2 & 1 & 6 & 3 & 6 & 3 & 0 & 9 \\ 4 & 2 & 1 & -6 & -3 & 6 & 3 & 0 & -9 \\ 4 & 2 & 1 & -6 & -3 & -6 & -3 & 0 & 9 \\ 4 & 2 & 1 & 6 & 3 & -6 & -3 & 0 & -9 \end{pmatrix}. \quad (\text{A1})$$

Then, the evolution of MRT-LB equation in velocity space and moment space are respectively express as follows

$$f_i(\mathbf{x} + \mathbf{e}_i \delta_t, t + \delta_t) = f_i(\mathbf{x}, t) + \sum_j (\mathbf{M}^{-1} \Gamma)_{ij} (m_j - m_j^{eq}) + \sum_j \left(\mathbf{M}^{-1} \left(\mathbf{I} - \frac{\Gamma}{2} \right) \right)_{ij} (C_j + S_j), \quad (\text{A2})$$

$$\mathbf{m}(\mathbf{x} + \mathbf{e}_i \delta_t, t + \delta_t) = \mathbf{m}(\mathbf{x}, t) - \Gamma (\mathbf{m}(\mathbf{x}, t) - \mathbf{m}^{eq}(\mathbf{x}, t)) + \left(\mathbf{I} - \frac{\Gamma}{2} \right) (\mathbf{C}(\mathbf{x}, t) + \mathbf{S}(\mathbf{x}, t)). \quad (\text{A3})$$

The moment function, the derivatives of time and space, as well as the source term and force term are expanded at consecutive scales of ϵ

$$\mathbf{m} = \mathbf{m}^{(0)} + \epsilon \mathbf{m}^{(1)} + \epsilon^2 \mathbf{m}^{(2)} + \dots, \quad \partial_t = \epsilon \partial_{t_1} + \epsilon^2 \partial_{t_2}, \quad \partial_\alpha = \epsilon \partial_{\alpha_1}, \quad \mathbf{C} = \epsilon \mathbf{C}^1, \quad \mathbf{S} = \epsilon \mathbf{S}^1, \quad (\text{A4})$$

where the external body force \mathbf{F}^B is ignored in \mathbf{S} for brevity; when $n > 0$, $m_0^{(n)} = (\phi \rho)^{(n)} = 0$, $m_4^{(n)} = j_x^{(n)} = -\delta_t F_x^p / 2$, $m_6^{(n)} = j_y^{(n)} = -\delta_t F_y^p / 2$ are obtained since $\phi \rho$ and $\phi \rho \mathbf{u}$ are conservative variables. Substituting the above expressions into Eq. (A3) and applying Taylor expansion, we can obtain the zero-, first-, and second-order equations in ϵ

$$\begin{aligned} \epsilon^0 : \mathbf{m}^{(0)} &= \mathbf{m}^{eq}, \\ \epsilon^1 : \tilde{\mathbf{D}}_1 \mathbf{m}^{(0)} &= -\Gamma' \mathbf{m}^{(0)} + \left(\mathbf{I} - \frac{\Gamma}{2} \right) \mathbf{M} (\mathbf{C}^1 + \mathbf{S}^1), \\ \epsilon^2 : \partial_{t_2} \mathbf{m}^{(0)} + \tilde{\mathbf{D}}_1 \left(\mathbf{I} - \frac{\Gamma}{2} \right) \mathbf{m}^{(1)} + \frac{\delta_t}{2} \tilde{\mathbf{D}}_1 \left(\mathbf{I} - \frac{\Gamma}{2} \right) \mathbf{M} (\mathbf{C}^1 + \mathbf{S}^1) &= -\Gamma' \mathbf{m}^{(2)}, \end{aligned} \quad (\text{A5})$$

where $\Gamma' = \Gamma / \delta_t$, $\tilde{\mathbf{D}}_1 = \mathbf{M} \mathbf{D}_1 \mathbf{M}^{-1} = \partial_{t_1} \mathbf{I} + \mathbf{E}_\alpha \partial_{\alpha_1}$, $\mathbf{D}_1 = \partial_{t_1} \mathbf{I} + \partial_{\alpha_1} \text{diag}(e_{0\alpha}, e_{1\alpha}, \dots, e_{8\alpha})$, and \mathbf{E}_α are explicitly provided in literature [41].

Based on above preparations, Eq. (A5) in ϵ^1 can be rewritten at t_1 time scale as

$$\begin{aligned}
& \partial_{t_1} \begin{pmatrix} \phi\rho \\ \phi\rho(-4+3u_x^2+3u_y^2+2X) \\ \phi\rho(4-3u_x^2-3u_y^2-3X) \\ \phi\rho u_x \\ (X-2)\phi\rho u_x \\ \phi\rho u_y \\ (X-2)\phi\rho u_y \\ \phi\rho(u_x^2-u_y^2) \\ \phi\rho u_x u_y \end{pmatrix} + \partial_{x_1} \begin{pmatrix} \phi\rho u_x \\ (X-1)\phi\rho u_x \\ (X-2)\phi\rho u_x \\ \kappa\rho c_s^2 + \phi\rho u_x^2 \\ -\kappa\rho c_s^2 - \phi\rho(u_x^2-u_y^2) \\ \phi\rho u_x u_y \\ \phi\rho u_x u_y \\ \phi\rho u_x u_y \\ -\kappa\rho c_s^2 u_x + \phi\rho u_x \\ \kappa\rho c_s^2 u_y \end{pmatrix} + \partial_{y_1} \begin{pmatrix} \phi\rho u_y \\ (X-1)\phi\rho u_y \\ (X-2)\phi\rho u_y \\ \phi\rho u_x u_y \\ \phi\rho u_x u_y \\ \kappa\rho c_s^2 + \phi\rho u_y^2 \\ -\kappa\rho c_s^2 + \phi\rho(u_x^2-u_y^2) \\ \kappa\rho c_s^2 u_y - \phi\rho u_y \\ \kappa\rho c_s^2 u_x \end{pmatrix} \\
& = \begin{pmatrix} 0 \\ -\tau'_e \varepsilon^{(1)} \\ -\tau'_e \varepsilon^{(1)} \\ \tau'_c \delta_t F_{x1}^p / 2 \\ -\tau'_q q_x^{(1)} \\ \tau'_c \delta_t F_{y1}^p / 2 \\ -\tau'_q q_y^{(1)} \\ -\tau'_v p_{xx}^{(1)} \\ -\tau'_v p_{xy}^{(1)} \end{pmatrix} + \begin{pmatrix} 0 \\ 6(1-\tau_e/2)(u_x F_{x1}^p + u_y F_{y1}^p) \\ -6(1-\tau_e/2)(u_x F_{x1}^p + u_y F_{y1}^p) \\ (1-\tau_c/2)F_{x1}^p \\ -(1-\tau_q/2)F_{x1}^p \\ (1-\tau_c/2)F_{y1}^p \\ -(1-\tau_q/2)F_{y1}^p \\ 2(1-\tau_v/2)(u_x F_{x1}^p - u_y F_{y1}^p) \\ (1-\tau_v/2)(u_x F_{y1}^p + u_y F_{x1}^p) \end{pmatrix} + \begin{pmatrix} 0 \\ (1-\tau_e/2)C_{a1} \\ 0 \\ 0 \\ 0 \\ 0 \\ 0 \\ (1-\tau_v/2)C_{b1} \\ (1-\tau_v/2)C_{c1} \end{pmatrix}, \tag{A6}
\end{aligned}$$

Similarly, Eq. (A5) in ε^2 can also be derived at t_2 time scale and the components corresponding to the conservative moments are given by

$$\begin{aligned}
& \partial_{t_2}(\phi\rho) = 0, \\
& \partial_{t_2}(\phi\rho u_x) - \frac{\delta_t}{2} \partial_{t_1} \left[(1-\frac{\tau_c}{2})F_{x1}^p \right] + \frac{1}{6} \partial_{x_1} \left[(1-\frac{\tau_e}{2})e^{(1)} \right] + \frac{1}{2} \partial_{x_1} \left[(1-\frac{\tau_v}{2})p_{xx}^{(1)} \right] + \partial_{y_1} \left[(1-\frac{\tau_v}{2})p_{xy}^{(1)} \right] \\
& + \frac{\delta_t}{2} \left\{ \partial_{t_1} \left[(1-\frac{\tau_c}{2})F_{x1}^p \right] + \partial_{x_1} \left[\frac{\tau_v}{2}(u_y F_{y1}^p - u_x F_{x1}^p) - \frac{\tau_e}{2}(u_x F_{x1}^p + u_y F_{y1}^p) + 2u_x F_{x1}^p \right] + \partial_{y_1} \left[(1-\frac{\tau_v}{2})(u_x F_{y1}^p + u_y F_{x1}^p) \right] \right\} \\
& + \frac{\delta_t}{2} \left\{ \frac{1}{6} \partial_{x_1} \left[(1-\frac{\tau_e}{2})C_{a1} \right] + \frac{1}{2} \partial_{x_1} \left[(1-\frac{\tau_v}{2})C_{b1} \right] + \partial_{y_1} \left[(1-\frac{\tau_v}{2})C_{c1} \right] \right\} = 0, \\
& \partial_{t_2}(\phi\rho u_y) - \frac{\delta_t}{2} \partial_{t_1} \left[(1-\frac{\tau_c}{2})F_{y1}^p \right] + \frac{1}{6} \partial_{y_1} \left[(1-\frac{\tau_e}{2})e^{(1)} \right] - \frac{1}{2} \partial_{y_1} \left[(1-\frac{\tau_v}{2})p_{xx}^{(1)} \right] + \partial_{x_1} \left[(1-\frac{\tau_v}{2})p_{xy}^{(1)} \right] \\
& + \frac{\delta_t}{2} \left\{ \partial_{t_1} \left[(1-\frac{\tau_c}{2})F_{y1}^p \right] + \partial_{y_1} \left[\frac{\tau_v}{2}(u_x F_{x1}^p - u_y F_{y1}^p) - \frac{\tau_e}{2}(u_x F_{x1}^p + u_y F_{y1}^p) + 2u_y F_{y1}^p \right] + \partial_{x_1} \left[(1-\frac{\tau_v}{2})(u_x F_{y1}^p + u_y F_{x1}^p) \right] \right\} \\
& + \frac{\delta_t}{2} \left\{ \frac{1}{6} \partial_{y_1} \left[(1-\frac{\tau_e}{2})C_{a1} \right] - \frac{1}{2} \partial_{y_1} \left[(1-\frac{\tau_v}{2})C_{b1} \right] + \partial_{x_1} \left[(1-\frac{\tau_v}{2})C_{c1} \right] \right\} = 0. \tag{A7}
\end{aligned}$$

Combining the correction force of Eq. (13) with the first, fourth, and sixth components of Eq. (A6), the macroscopic governing equations at t_1 time scale can be derived

$$\begin{aligned}
& \partial_{t_1}(\phi\rho) + \partial_{x_1}(\phi\rho u_x) + \partial_{y_1}(\phi\rho u_y) = 0, \\
& \partial_{t_1}(\phi\rho u_x) + \partial_{x_1}(\phi\rho u_x u_x) + \partial_{y_1}(\phi\rho u_x u_y) = -\phi \partial_{x_1}(\rho c_s^2), \\
& \partial_{t_1}(\phi\rho u_y) + \partial_{x_1}(\phi\rho u_x u_y) + \partial_{y_1}(\phi\rho u_y u_y) = -\phi \partial_{y_1}(\rho c_s^2). \tag{A8}
\end{aligned}$$

Subsequently, neglecting the term of order $O(|\mathbf{u}|^3)$ and higher-order terms of $u_\beta \partial_\alpha (u_\alpha u_\beta)$ under the incompressible condition, the expressions of $e^{(1)}$, $p_{xx}^{(1)}$ and $p_{xy}^{(1)}$ in Eq. (A7) can be obtained from the second, eighth, and ninth components of Eq. (A6)

$$\begin{aligned}
-\tau'_e e^{(1)} &= -2\kappa(u_x \partial_{x1} \rho + u_y \partial_{y1} \rho) + \kappa[\partial_{x1}(\rho u_x) + \partial_{y1}(\rho u_y)] \\
&+ 3[\partial_{x1}(\phi \rho u_x) + \partial_{y1}(\phi \rho u_y)] + 2\kappa \partial_{t1} \rho + 3\tau_e(u_x F_{x1}^p + u_y F_{y1}^p) + \left(\frac{\tau_e}{2} - 1\right) C_{a1}, \\
-\tau'_v p_{xx}^{(1)} &= -\frac{2\kappa}{3}(u_x \partial_{x1} \rho - u_y \partial_{y1} \rho) - \frac{\kappa}{3}[\partial_{x1}(\rho u_x) - \partial_{y1}(\rho u_y)] \\
&+ [\partial_{x1}(\phi \rho u_x) - \partial_{y1}(\phi \rho u_y)] + \tau_v(u_x F_{x1}^p - u_y F_{y1}^p) + \left(\frac{\tau_v}{2} - 1\right) C_{b1}, \\
-\tau'_v p_{xy}^{(1)} &= \frac{\kappa}{3} \rho(\partial_{x1} u_y + \partial_{y1} u_x) + \frac{\tau_v}{2}(u_x F_{y1}^p + u_y F_{x1}^p) + \left(\frac{\tau_v}{2} - 1\right) C_{c1},
\end{aligned} \tag{A9}$$

where no expression is provided for the time derivative of ρ , so we replace it with the known partial derivatives, i.e., $\partial_{t1} \rho = (\partial_{t1}(\phi \rho) - \rho \partial_{t1} \phi) / \phi = -(\partial_{x1}(\phi \rho u_x) + \partial_{y1}(\phi \rho u_y) + \rho \partial_{t1} \phi) / \phi$. Then, substituting the penalty terms of Eq. (20) into Eq. (A9), $e^{(1)}$, $p_{xx}^{(1)}$ and $p_{xy}^{(1)}$ related to the viscosity stress tensor are successfully corrected

$$\begin{aligned}
-\tau'_e e^{(1)} &= 2\phi \rho(\partial_{x1} u_x + \partial_{y1} u_y) + 3\tau_e(u_x F_{x1}^p + u_y F_{y1}^p) + \frac{\tau_e}{2} C_{a1}, \\
-\tau'_v p_{xx}^{(1)} &= \frac{2}{3} \phi \rho(\partial_{x1} u_x - \partial_{y1} u_y) + \tau_v(u_x F_{x1}^p - u_y F_{y1}^p) + \frac{\tau_v}{2} C_{b1}, \\
-\tau'_v p_{xy}^{(1)} &= \frac{1}{3} \phi \rho(\partial_{x1} u_y + \partial_{y1} u_x) + \frac{\tau_v}{2}(u_x F_{y1}^p + u_y F_{x1}^p) + \frac{\tau_v}{2} C_{c1}.
\end{aligned} \tag{A10}$$

Then, substituting Eq. (A10) into Eq. (A7), the macroscopic governing equations at t_2 time scale can be derived

$$\begin{aligned}
\partial_{t2}(\phi \rho) &= 0, \\
\partial_{t2}(\phi \rho u_x) &= \partial_{x1}[\phi \rho v(\partial_{x1} u_x - \partial_{y1} u_y)] + \partial_{y1}[\phi \rho v(\partial_{x1} u_y + \partial_{y1} u_x)] + \partial_{x1}[\phi \rho v_e(\partial_{x1} u_x + \partial_{y1} u_y)], \\
\partial_{t2}(\phi \rho u_y) &= \partial_{x1}[\phi \rho v(\partial_{x1} u_y + \partial_{y1} u_x)] + \partial_{y1}[\phi \rho v(\partial_{y1} u_y - \partial_{x1} u_x)] + \partial_{y1}[\phi \rho v_e(\partial_{x1} u_x + \partial_{y1} u_y)],
\end{aligned} \tag{A11}$$

where $\nu = c_s^2(\tau_v^{-1} - 0.5)\delta_t$, $\nu_e = c_s^2(\tau_e^{-1} - 0.5)\delta_t$ are the kinematic shear and bulk viscosities.

Lastly, combining the equations at t_1 and t_2 time scales together, i.e., Eqs. (A8) and (A11), we recover the macroscopic equations as follows

$$\begin{aligned}
\partial_t(\phi \rho) + \nabla \cdot (\phi \rho \mathbf{u}) &= 0, \\
\partial_t(\phi \rho \mathbf{u}) + \nabla \cdot (\phi \rho \mathbf{u} \mathbf{u}) &= -\phi \nabla p + \nabla \cdot (\phi \boldsymbol{\tau}),
\end{aligned} \tag{A12}$$

where $p = \rho c_s^2$ is the pressure term, $\boldsymbol{\tau} = \rho v(\nabla \mathbf{u} + (\nabla \mathbf{u})^T) + \rho(\nu_e - \nu)(\nabla \cdot \mathbf{u})\mathbf{I}$ is the viscous stress tensor, and the target VANSE of Eq. (1) is exactly recovered when $\nu_e = \nu/3$ is chosen.

Appendix B. MRTLB-VANSE with the second-order equilibrium distribution

The second-order density equilibrium function from the Hermite expansion

$$f_i^{eq}(\mathbf{x}, t) = \begin{cases} \phi\rho - \sum_{i \neq 0} \omega_i \kappa \rho - \omega_0 \phi \rho \frac{\mathbf{u} \cdot \mathbf{u}}{2c_s^2}, & i = 0 \\ \omega_i \left(\kappa \rho + \phi \rho \left(\frac{\mathbf{e}_i \cdot \mathbf{u}}{c_s^2} + \frac{(\mathbf{e}_i \cdot \mathbf{u})^2}{2c_s^4} - \frac{\mathbf{u} \cdot \mathbf{u}}{2c_s^2} \right) \right), & i = 1 \sim 8 \end{cases} \quad (\text{B1})$$

The equilibrium moment

$$\mathbf{m}^{eq} = \mathbf{M} \mathbf{f}^{eq} = (m_0^{eq}, m_1^{eq}, \dots, m_8^{eq})^T = \phi \rho (1, -4 + 3\mathbf{u}^2 + 2X, 4 - 3\mathbf{u}^2 - 3X, u_x, -u_x, u_y, -u_y, u_x^2 - u_y^2, u_x u_y)^T. \quad (\text{B2})$$

The penalty source term for viscous stress

$$\begin{aligned} C_a &= -2\kappa[\partial_{x1}(\rho u_x) + \partial_{y1}(\rho u_y)] + 2(\kappa - \phi)\rho(\partial_{x1}u_x + \partial_{y1}u_y) \\ &\quad + (4 - 2X)[\partial_{x1}(\phi \rho u_x) + \partial_{y1}(\phi \rho u_y)] - 2X\rho\partial_{t1}\phi, \\ C_b &= -\frac{2}{3}\kappa[\partial_{x1}(\rho u_x) - \partial_{y1}(\rho u_y)] + \frac{2}{3}(\kappa - \phi)\rho(\partial_{x1}u_x - \partial_{y1}u_y) \\ &\quad + \frac{2}{3}[\partial_{x1}(\phi \rho u_x) - \partial_{y1}(\phi \rho u_y)], \\ C_c &= -\frac{\kappa}{3}[\partial_{x1}(\rho u_y) + \partial_{y1}(\rho u_x)] + \frac{1}{3}(\kappa - \phi)\rho(\partial_{x1}u_y + \partial_{y1}u_x) \\ &\quad + \frac{1}{3}[\partial_{x1}(\phi \rho u_y) + \partial_{y1}(\phi \rho u_x)]. \end{aligned} \quad (\text{B3})$$

Appendix C. MMS body forces

Case I:

$$\begin{aligned} F_x^B &= \frac{2\pi u_s^2 \tilde{\phi}}{n^3} \sin^3(\pi x^*) \cos(\pi x^*) \sin^2(\pi y^*) + \frac{4\nu\pi^2 u_s b}{n^3} \sin^3(\pi x^*) \cos^3(\pi y^*) \\ &\quad + \frac{4\nu\pi^2 u_s}{n^3} \sin(\pi y^*) \cos(\pi y^*) \left(\begin{aligned} &-6\tilde{\phi} \sin^2(\pi x^*) + 2a \cos^2(\pi x^*) \\ &+ 5b \sin(\pi x^*) \cos^2(\pi x^*) \sin(\pi y^*) \end{aligned} \right) \\ F_y^B &= \frac{2\pi u_s^2 \tilde{\phi}}{n^3} \sin^2(\pi x^*) \sin^3(\pi y^*) \cos(\pi y^*) \\ &\quad - \frac{4\nu\pi^2 u_s}{n^3} \sin(\pi x^*) \cos(\pi x^*) \cos^2(\pi y^*) (2a + 5b \sin(\pi x^*) \sin(\pi y^*)) \\ &\quad + \frac{4\nu\pi^2 u_s}{n^3} \cos(\pi x^*) \sin^2(\pi y^*) \left(\begin{aligned} &6a \sin(\pi x^*) + 6b \sin^2(\pi x^*) \sin(\pi y^*) \\ &-b \cos^2(\pi x^*) \sin(\pi y^*) \end{aligned} \right) \end{aligned} \quad (\text{C1})$$

Case II:

$$\begin{aligned} F_x^B &= F_y^B = \frac{2\pi u_s^2 ab}{n^3} \exp(b \sin(\pi x^*) \sin(\pi y^*)) \sin(\pi(x^* + y^*)) \\ &\quad - \frac{4\nu\pi^2 u_s ab}{3n^3} (\cos(\pi x^*) \cos(\pi y^*) - 7 \sin(\pi x^*) \sin(\pi y^*)) \end{aligned} \quad (\text{C2})$$

Case III:

$$\begin{aligned}
F_x^B &= -\frac{8\pi u_s^2 b}{n^3} \sin(\pi(x_i^* + y_i^*)) + \frac{2\pi u_s^2 b}{n^3 \tilde{\phi}^2} \sin(\pi(x_i^* + y_i^*)) (4\tilde{\phi}^2 - 1) \\
&+ \frac{2\nu\pi^2 u_s b}{3n^3 \tilde{\phi}^2} \left(\begin{aligned} &3b \cos(2\pi x_i^*) + 4b \cos(2\pi y_i^*) - 7b \\ &+ 8a \cos(\pi(x_i^* + y_i^*)) - 6a \cos(\pi(x_i^* - y_i^*)) \end{aligned} \right) \\
F_y^B &= -\frac{8\pi u_s^2 b}{n^3} \sin(\pi(x_i^* + y_i^*)) + \frac{2\pi u_s^2 b}{n^3 \tilde{\phi}^2} \sin(\pi(x_i^* + y_i^*)) (4\tilde{\phi}^2 - 1) \\
&+ \frac{2\nu\pi^2 u_s b}{3n^3 \tilde{\phi}^2} \left(\begin{aligned} &4b \cos(2\pi x_i^*) + 3b \cos(2\pi y_i^*) - 7b \\ &+ 8a \cos(\pi(x_i^* + y_i^*)) - 6a \cos(\pi(x_i^* - y_i^*)) \end{aligned} \right)
\end{aligned} \tag{C3}$$

References

- [1] S. Fu, Z. Hao, L. Wang, A pressure-based lattice Boltzmann method for the volume-averaged Navier-Stokes equations, *J. Comput. Phys.*, 516 (2024).
- [2] J. Zhang, L. Wang, J. Ouyang, Lattice Boltzmann model for the volume-averaged Navier-Stokes equations, *EPL (Europhysics Letters)*, 107 (2014).
- [3] B. Blais, J.-M. Tucny, D. Vidal, F. Bertrand, A conservative lattice Boltzmann model for the volume-averaged Navier–Stokes equations based on a novel collision operator, *J. Comput. Phys.*, 294 (2015) 258-273.
- [4] F. Bukreev, S. Simonis, A. Kummerländer, J. Jeßberger, M.J. Krause, Consistent lattice Boltzmann methods for the volume averaged Navier–Stokes equations, *J. Comput. Phys.*, 490 (2023).
- [5] Z.Y. Zhou, S.B. Kuang, K.W. Chu, A.B. Yu, Discrete particle simulation of particle–fluid flow: model formulations and their applicability, *J. Fluid Mech.*, 661 (2010) 482-510.
- [6] D. Gidaspow, *Multiphase Flow and Fluidization: Continuum and Kinetic Theory Descriptions*, Academic Press, 1994.
- [7] S. Golshan, R. Sotudeh-Gharebagh, R. Zarghami, N. Mostoufi, B. Blais, J.A.M. Kuipers, Review and implementation of CFD-DEM applied to chemical process systems, *Chem. Eng. Sci.*, 221 (2020).
- [8] D.M. Snider, An incompressible three-dimensional multiphase particle-in-cell model for dense particle flows, *J. Comput. Phys.*, 170 (2001) 523-549.
- [9] S. Wang, Y. Shen, Coarse-grained CFD-DEM modelling of dense gas-solid reacting flow, *International Journal of Heat and Mass Transfer*, 184 (2022).
- [10] W.T. Wu, F. Yang, J.F. Antaki, N. Aubry, M. Massoudi, Study of blood flow in several benchmark micro-channels using a two-fluid approach, *Int. J. Eng. Sci.*, 95 (2015) 49-59.
- [11] Y.-J. Chou, S.-H. Gu, Y.-C. Shao, An Euler–Lagrange model for simulating fine particle suspension in liquid flows, *J. Comput. Phys.*, 299 (2015) 955-973.
- [12] F.J. Carrillo, I.C. Bourg, C. Soulaïne, Multiphase flow modeling in multiscale porous media: An open-source micro-continuum approach, *Journal of Computational Physics: X*, 8 (2020).
- [13] C. Soulaïne, S. Roman, A. Kavscek, H.A. Tchelepi, Pore-scale modelling of multiphase reactive flow: application to mineral dissolution with production of CO₂, *J. Fluid Mech.*, 855 (2018) 616-645.
- [14] Q. Xu, X. Dai, J. Yang, Z. Liu, L. Shi, Image-based modelling of coke combustion in a multiscale porous medium using a micro-continuum framework, *J. Fluid Mech.*, 932 (2021).

- [15] F.J. Carrillo, I.C. Bourg, Modeling Multiphase Flow Within and Around Deformable Porous Materials: A Darcy-Brinkman-Biot Approach, *Water Resources Research*, 57 (2021) 27.
- [16] F.J. Carrillo, I.C. Bourg, Capillary and viscous fracturing during drainage in porous media, *Physical Review E*, 103 (2021) 10.
- [17] T. Kruger, H. Kusumaatmaja, A. Kuzmin, O. Shardt, G. Silva, E.M. Viggien, Lattice Boltzmann Method: Principles and Practice, in: *Lattice Boltzmann Method: Principles and Practice*, Springer International Publishing Ag, Cham, 2017, pp. 1-694.
- [18] M.P. Lautenschlaeger, J. Weinmiller, B. Kellers, T. Danner, A. Latz, Homogenized lattice Boltzmann model for simulating multi-phase flows in heterogeneous porous media, *Advances in Water Resources*, 170 (2022).
- [19] J. Zhu, J. Ma, An improved gray lattice Boltzmann model for simulating fluid flow in multi-scale porous media, *Advances in Water Resources*, 56 (2013) 61-76.
- [20] G.G. Pereira, Grayscale lattice Boltzmann model for multiphase heterogeneous flow through porous media, *Physical Review E*, 93 (2016) 063301.
- [21] I. Ginzburg, Comment on “An improved gray Lattice Boltzmann model for simulating fluid flow in multi-scale porous media”: Intrinsic links between LBE Brinkman schemes, *Advances in Water Resources*, 88 (2016) 241-249.
- [22] Z. Guo, T.S. Zhao, Lattice Boltzmann model for incompressible flows through porous media, *Phys Rev E Stat Nonlin Soft Matter Phys*, 66 (2002) 036304.
- [23] Y. Liu, J. Feng, J. Min, X. Zhang, Homogenized color-gradient lattice Boltzmann model for immiscible two-phase flow in multiscale porous media, *Journal of Applied Physics*, 135 (2024).
- [24] L. Wang, L.-P. Wang, Z. Guo, J. Mi, Volume-averaged macroscopic equation for fluid flow in moving porous media, *International Journal of Heat and Mass Transfer*, 82 (2015) 357-368.
- [25] S. Zhang, T. Jiang, H. Huang, L.-J. Huang, L.-Z. Zhang, Lattice Boltzmann model for predicting frosting process on surfaces considering wettability, *Physical Review E*, 107 (2023).
- [26] T.F. Wang, J.F. Wang, Two-fluid model based on the lattice Boltzmann equation, *Physical Review E*, 71 (2005) 4.
- [27] F. Song, W. Wang, J. Li, A lattice Boltzmann method for particle-fluid two-phase flow, *Chem. Eng. Sci.*, 102 (2013) 442-450.
- [28] Q. Li, G. Yang, Y. Huang, X. Lu, J. Min, M. Wang, Lattice Boltzmann method for particulate multiphase flow system, *International Journal of Mechanical Sciences*, 273 (2024).
- [29] S.B. Höcker, R. Trunk, W. Dörfler, M.J. Krause, Towards the simulations of inertial dense particulate flows with a volume-averaged lattice Boltzmann method, *Computers & Fluids*, 166 (2018) 152-162.
- [30] M.L. Maier, R.A. Patel, N.I. Prasianakis, S.V. Churakov, H. Nirschl, M.J. Krause, Coupling of multiscale lattice Boltzmann discrete-element method for reactive particle fluid flows, *Physical Review E*, 103 (2021) 033306.
- [31] Q. Li, K.H. Luo, Y.L. He, Y.J. Gao, W.Q. Tao, Coupling lattice Boltzmann model for simulation of thermal flows on standard lattices, *Phys Rev E Stat Nonlin Soft Matter Phys*, 85 (2012) 016710.
- [32] Q. Li, Y. Yu, R.Z. Huang, Achieving thermodynamic consistency in a class of free-energy multiphase lattice Boltzmann models, *Physical Review E*, 103 (2021) 013304.
- [33] Z.L. Guo, C.G. Zheng, B.C. Shi, Discrete lattice effects on the forcing term in the lattice

Boltzmann method, *Physical Review E*, 65 (2002) 6.

[34] R. Huang, H. Wu, Third-order analysis of pseudopotential lattice Boltzmann model for multiphase flow, *J. Comput. Phys.*, 327 (2016) 121-139.

[35] A. Kumar, Isotropic finite-differences, *J. Comput. Phys.*, 201 (2004) 109-118.

[36] X. Shan, X.-F. Yuan, H. Chen, Kinetic theory representation of hydrodynamics: a way beyond the Navier–Stokes equation, *J. Fluid Mech.*, 550 (2006).

[37] Y. Ba, H. Liu, Q. Li, Q. Kang, J. Sun, Multiple-relaxation-time color-gradient lattice Boltzmann model for simulating two-phase flows with high density ratio, *Physical Review E*, 94 (2016).

[38] H. Liu, A.J. Valocchi, Q. Kang, Three-dimensional lattice Boltzmann model for immiscible two-phase flow simulations, *Phys Rev E Stat Nonlin Soft Matter Phys*, 85 (2012) 046309.

[39] H. Huang, J.-J. Huang, X.-Y. Lu, M.C. Sukop, On Simulations of High-Density Ratio Flows Using Color-Gradient Multiphase Lattice Boltzmann Models, *Int. J. Mod. Phys. C*, 24 (2013).

[40] Z.X. Wen, Q. Li, Y. Yu, K.H. Luo, Improved three-dimensional color-gradient lattice Boltzmann model for immiscible two-phase flows, *Physical Review E*, 100 (2019) 023301.

[41] Y. Liu, J. Min, X. Zhang, A novel micro-continuum lattice Boltzmann approach for multiscale modeling immiscible two-phase flow in porous media, *Physics of Fluids*, 36 (2024).

[42] P. Lallemand, L.-S. Luo, Theory of the lattice Boltzmann method: Dispersion, dissipation, isotropy, Galilean invariance, and stability, *Physical Review E*, 61 (2000) 6546-6562.

[43] L. Yang, X. Li, Y. Yang, S. Qin, G. Hou, J. Qin, A consistent generalized model-based lattice Boltzmann flux solver for incompressible porous flows, *Physics of Fluids*, 36 (2024).

[44] L. Ju, B.C. Shan, Z. Yang, Z.L. Guo, An exact non-equilibrium extrapolation scheme for pressure and velocity boundary conditions with large gradients in the lattice Boltzmann method, *Computers & Fluids*, 231 (2021) 10.

[45] B. Blais, F. Bertrand, On the use of the method of manufactured solutions for the verification of CFD codes for the volume-averaged Navier–Stokes equations, *Computers & Fluids*, 114 (2015) 121-129.

[46] T.E. Geitani, S. Golshan, B. Blais, A high-order stabilized solver for the volume averaged Navier-Stokes equations, *Int. J. Numer. Methods Fluids*, 95 (2023) 1011-1033.